technologies

MDPI

Article

ZnO Nanoparticles by Hydrothermal Method: Synthesis and Characterization

Juan Carlos Anaya-Zavaleta [1], Antonio Serguei Ledezma-Pérez [2], Carlos Gallardo-Vega [2], Joelis Rodríguez-Hernández [2], Carmen Natividad Alvarado-Canché [2], Perla Elvia García-Casillas [2], Arxel de León [3,*] and Agustín Leobardo Herrera-May [1,4,*]

1 Micro and Nanotechnology Research Center, Universidad Veracruzana, Boca del Río 94294, Veracruz, Mexico; juancarlosanayazavaleta@gmail.com
2 Centro de Investigación en Química Aplicada, Saltillo 25294, Coahuila, Mexico; antonio.ledezma@ciqa.edu.mx (A.S.L.-P.); carlos.gallardo@ciqa.edu.mx (C.G.-V.); joelis.rodriguez@ciqa.edu.mx (J.R.-H.); carmen.alvarado@ciqa.edu.mx (C.N.A.-C.); perla.garcia@ciqa.edu.mx (P.E.G.-C.)
3 CONAHCYT-Centro de Investigación en Química Aplicada, Saltillo 25294, Coahuila, Mexico
4 Facultad de Ingeniería de la Construcción y el Hábitat, Universidad Veracruzana, Boca del Río 94294, Veracruz, Mexico
* Correspondence: arxel.deleon@ciqa.edu.mx (A.d.L.); leherrera@uv.mx (A.L.H.-M.); Tel.: +52-2297752000 (A.L.H.-M.)

Abstract: The synthesis of reliable, cost-effective, and eco-friendly ZnO piezoelectric nanoparticles (NPs) can contribute to nanotechnology applications in electronics, sensors, and energy harvesting. Herein, ZnO NPs were synthesized using a hydrothermal method under varied reaction times and adding ammonium hydroxide, which provided an advantage of a low-cost, scalable, low-temperature, and environmentally friendly process. Characterization through UV–Vis spectroscopy revealed absorption peaks between 374 and 397 nm, showing a blue shift compared to bulk ZnO (400 nm) attributable to nanoscale dimensions. Transmission Electron Microscopy (TEM) analysis indicated particle dimensions with length and width ranges from 150 to 341 nm and from 83 to 120 nm, respectively. X-ray diffraction (XRD) confirmed high-crystalline quality, with crystallite sizes calculated using the Scherrer equation. In addition, the effective mass model provided an estimated band gap that matched with the reported data. Also, the lattice parameters, interplanar distances, and Zn-O bond lengths were consistent with Joint Committee on Powder Diffraction Standards (JCPDS). Finally, a ZnO NP film was deposited on a steel substrate, which generated a displacement of 150 nm under a square wave voltage of 10 V. The piezoelectric behavior of the synthesized ZnO NPs can be useful for fabrication of piezoelectric nanogenerators. The proposed synthesis can allow ZnO NPs with potential application in electronic devices, energy harvesters, and transducers.

Keywords: nanoparticles synthesis; energy harvesters; hydrothermal method; piezoelectric nanogenerators; ZnO nanoparticles

check for updates

Academic Editors: Xavier Fernando, Manoj Gupta, Pratheepa Jeganathan and Nades Palaniyar

Received: 5 November 2024
Revised: 15 December 2024
Accepted: 24 December 2024
Published: 1 January 2025

Citation: Anaya-Zavaleta, J.C.; Ledezma-Pérez, A.S.; Gallardo-Vega, C.; Rodríguez-Hernández, J.; Alvarado-Canché, C.N.; García-Casillas, P.E.; de León, A.; Herrera-May, A.L. ZnO Nanoparticles by Hydrothermal Method: Synthesis and Characterization. *Technologies* **2025**, *13*, 18. https://doi.org/10.3390/technologies13010018

Copyright: © 2025 by the authors. Licensee MDPI, Basel, Switzerland. This article is an open access article distributed under the terms and conditions of the Creative Commons Attribution (CC BY) license (https://creativecommons.org/licenses/by/4.0/).

1. Introduction

The synthesis of zinc oxide (ZnO) nanoparticles (NPs) has gained significant scientific interest due to the unique chemical and physical properties of these NPs that arise specifically at the nanoscale. Unlike bulk materials, nanoparticles exhibit a high surface-area-to-volume ratio, providing increased surface contact sites that are crucial for catalytic, sensor, and energy applications [1]. However, the synthesis of ZnO NPs with precise size,

morphology, and crystallinity is a challenge. In addition, the synthesis of these nanoparticles requires a scalable and cost-effective process with minimum environmental impact. Variations in synthesis conditions (e.g., temperature, pH, and precursor concentration) can drastically alter nanoparticle morphology and functionality. Therefore, synthesis of optimal parameters is necessary to achieve desired properties of nanoparticles for specific applications. Furthermore, the reproducible and controlled formation of ZnO NPs can allow the fabrication of ZnO films for applications in piezoelectric devices and sensors, in which the nanoparticle size and shape affect their performance.

ZnO is an *n*-type semiconductor from Groups II–VI which can have three different structures: wurtzite (hexagonal structure), zinc blende (cubic), and rock salt (cubic) [2]. The ZnO wurtzite is the most stable structure with lattice constants of $a = 3.2498$ Å and $c = 5.2066$. In the wurtzite structure, the Zn^{2+} cation is surrounded by four O^{2-} anions and vice versa. This tetrahedral atomic arrangement is non-centrosymmetric in the ZnO crystal structure. When unstressed, the centers of mass of the positive and negative ions coincide at the center of the tetrahedron. There is no net polarization in the unit cell. Upon the application of pressure at an apex of the tetrahedron, the centers of mass of the cations and anions are relatively displaced, making the generation of a net polarization or charges on the crystal surface [3]. ZnO is an abundant natural metal oxide, chemically stable in air, low-cost and biologically safe with a wide band gap (3.37 eV), and large exciton binding energy (60 meV) [4,5]. These properties of ZnO NPs allow their application in nanogenerators [6,7], solar cells [8,9], photocatalysis [10], electrochemiluminescence [11], and gas sensors [12,13].

There are several methods for ZnO synthesis such as hydrothermal [14,15], laser ablation [16], microwave [17], chemical vapor deposition [18], electrochemical [19], and sol–gel [20], among others. Moreover, ZnO nanostructures can be synthesized as nanoparticles [21], nanorods [22], nanobelts [23], nanosheets [24], nanotubes [25], and nanowires [26]. It is due the relation between properties and morphology of the ZnO nanostructures.

Herein, we propose a cost-effective, low-cost, scalable, and eco-friendly hydrothermal synthesis method for producing high-quality ZnO nanoparticles at a low temperature (150 °C) under variable reaction times. By adjusting the reaction conditions and adding ammonium hydroxide in select cases, we investigate the effects of hydroxide concentration on the morphology, crystallite size, band gap, and lattice parameters of the ZnO nanoparticles. The low strain observed with lattice parameter measurements for ZnO NPs confirms the stability and structural quality of the synthesized ZnO NPs, which are demonstrated by their XRD patterns and stable electrical properties. Furthermore, we study the ZnO NPs synthesis routes using Transmission Electron Microscopy (TEM), UV–Vis spectroscopy, X-ray Diffraction (XRD), and electrical behavior via hysteresis loops. These measurements of the ZnO nanoparticles show the versatility and robustness of the proposed synthesis. By using a fotonic sensor, we measure the displacements of a ZnO NPs under square wave voltages from 1 to 10 V. Thus, we report the relationships of the synthesis-structure properties of ZnO nanoparticles, which allow a scalable and sustainable method for fabrication of ZnO NPs. These ZnO nanoparticles have potential applications in piezoelectric nanogenerators, sensors, transducers, and consumer electronics.

2. Materials and Methods

2.1. Materials

Zinc acetate dihydrate ($Zn(CH_3COO)_2{\cdot}2H_2O$) from the Sigma-Aldrich chemical company (St. Louis, MO, USA), ethylenglycol (solvent 99.8%), isopropyl alcohol (solvent 99.9%), and deionized water with a concentration of 1 M of ammonium hydroxide (30% of concentration in the container) were purchased from J.T. Baker.

2.2. ZnO Synthesis by Hydrothermal Method

The ZnO nanoparticles were synthesized by a modified methodology of Elvira-Hernández et al. [27]. We employed a hydrothermal method, which is one of the most widely used synthesis methods for the growth of ZnO nanorods due to its low cost and low temperature [28]. The reactions were placed in a beaker that was subsequently mixed with a magnetic stirring until all components were completely dissolved (see Figure 1a,b). The solution had 500 mg of zinc acetate dihydrate dissolved in 10 mL of ethylene glycol and 3 mL of deionized water for each reaction. For reactions with (*), the ammonium hydroxide was used, 50 microliters of deionized water with a 1 M of ammonium hydroxide concentration. This mixture was stirred in magnetic stirring for 20 h to completely dissolve the zinc acetate. After this, the solutions were put into a Teflon-lined stainless steel autoclave and left to react (see Figure 1c). Table 1 shows the temperature and time for each reaction. The products were centrifuged and washed with isopropyl alcohol thrice at 15,000 rpm for 15 min (see Figure 1d).

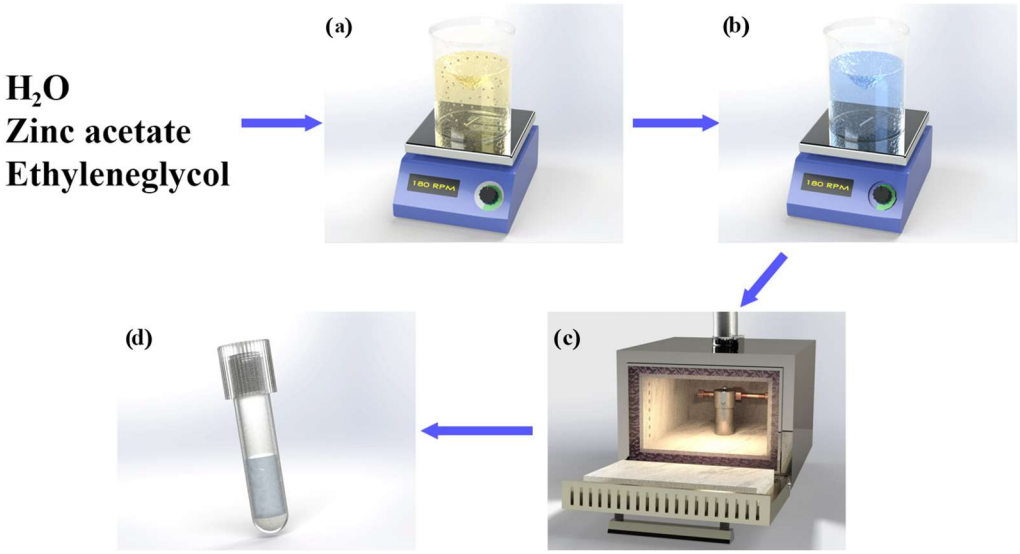


Figure 1. Reaction methodology: (**a**) solution on a magnetic stirring, (**b**) completely dissolved solution, (**c**) solution into a Teflon-lined stainless steel autoclave in a muffle, and (**d**) washed and centrifuged.

Table 1. Temperature and time for each reaction.

Reaction	Temperature (°C)	Time (Min)
ZnO-1	150	90
*ZnO-1	150	90
ZnO-2	150	180
*ZnO-2	150	180
ZnO-3	150	360

Note: For reactions with (*), the ammonium hydroxide was used.

The thermal and high-pressure conditions produced in the reactor by ethylene glycol can dissociate the zinc acetate, generating Zn^{2+} ions, and the acetate ions react with the water, forming acetic acid and hydroxyl ions. The hydroxyl ions can bind with the Zn^{2+}, producing zinc hydroxide that can generate oversaturated nucleation points and precipitate in more stable species for temperature and reaction time. The Zn(OH) dehydrates and produces ZnO that nucleates in a heterogeneous system [29]. The ammonium hydroxide

can produce more hydroxyl ions, favoring the Zn(OH) and decreasing the growth time of ZnO.

$$2Zn(CH_3COO)_2 \cdot 2H_2O \rightarrow 2Zn^{2+} + 4(CH_3COO)^- + 4H_2O$$

$$4(CH_3COO)^- + 4H_2O \rightarrow 4CH_3COOH + 4OH^-$$

$$2Zn^{2+} + 4OH^- \rightarrow Zn_2(OH)_4$$

$$Zn_2(OH)_4 \rightarrow 2ZnO$$

2.3. Characterization Methods

UV–Vis spectroscopy was collected with a Shimadzu UV-2401PC spectrophotometer (Shimadzu, Kyoto, Japan) at room temperature; the ZnO nanoparticles were dispersed in isopropyl alcohol. Powder X-ray diffraction measurements were made with KαCu (λ = 1.54183 Å) using a Ni filter Ultima IV (Rigaku, Tokyo, Japan), operated in a Bragg–Brentano geometry with 40 kV voltage and 44 mA of emission current, equipped with a D/tex Ultra detector. The diffraction patterns were registered in an angular interval from 20° to 80° at 2θ with an angular resolution of 0.02° and velocity of 10°/min. The powder was put on a glass holder sample. The morphological study was realized by transmission electron microscopy with a TITAN microscope supplied by FEI-Company (Hillsboro, OR, USA). The samples were prepared with a few drops of ZnO redispersed in isopropyl alcohol (0.1 mg/mL) on a lacey carbon grid. Finally, the electrical behavior was characterized by the Precision PiezoMEMS tester for Radiant Technologies, Inc. (Albuquerque, NM, USA) equipment.

3. Results and Discussion

3.1. UV–Vis

The formation of nanoparticles was carried out by dissociation in the zinc acetate, generating Zn and acetate ions. When the acetate ions are protonated with water, they form acetic acid and hydroxyl ions. The hydroxyl ions join the Zn^{2+} ion producing a zinc hydroxide; with the help of the temperature of the medium and the reaction time, upon dehydration ZnO is generated. Moreover, the relative surface activities of various growth facets under given conditions determine the surface morphology of the grown ZnO structure [29]. Finally, the size and shape of the nanoparticles can affect the properties of the materials [30]. The absorption spectrum obtained had a blue shift compared to the bulk material due to these factors. Figure 2 shows the absorption spectrum from each ZnO NP reaction, with ZnO synthesis peaks observed between 374 and 397 nm. It is attributed to ZnO (see Table 2). The absorption peak was generally centered between 374 and 379 nm in all samples. Only one sample had a bathochromic shift. This contribution is due to the easy nucleation favored for ammonium hydroxide, which increases the size of the structure and agglomerates due to the increase in hydroxyl groups.

Table 2. Maximum absorption peak values from each ZnO nanoparticle reaction.

Reaction	Maximum Value Peak
ZnO-1	379 nm
*ZnO-1	374 nm
ZnO-2	376 nm
*ZnO-2	387–397 nm
ZnO-3	377 nm

Note: For reactions with (*), the ammonium hydroxide was used.

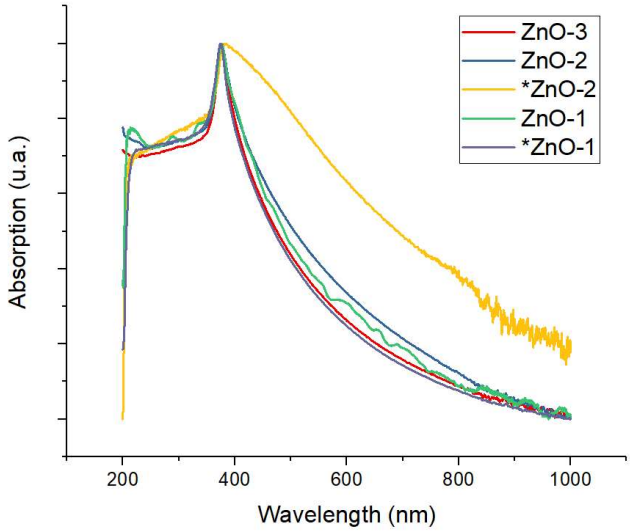


Figure 2. Normalized UV–Vis absorbance from each ZnO nanoparticle reaction. Note: For reactions with (*), the ammonium hydroxide was used.

3.2. TEM

The TEM images (Figure 3a–e) show the width and large histograms of the size distribution of each reaction, confirming the particle formation at the nanoscale. These nanoparticles were corroborated with free software ImageJ (https://imagej.net/ij/) and measured in length and width. The mean length and width of the ZnO nanoparticles are around 150 to 341 nm and 72 to 120 nm, respectively (see Table 3).

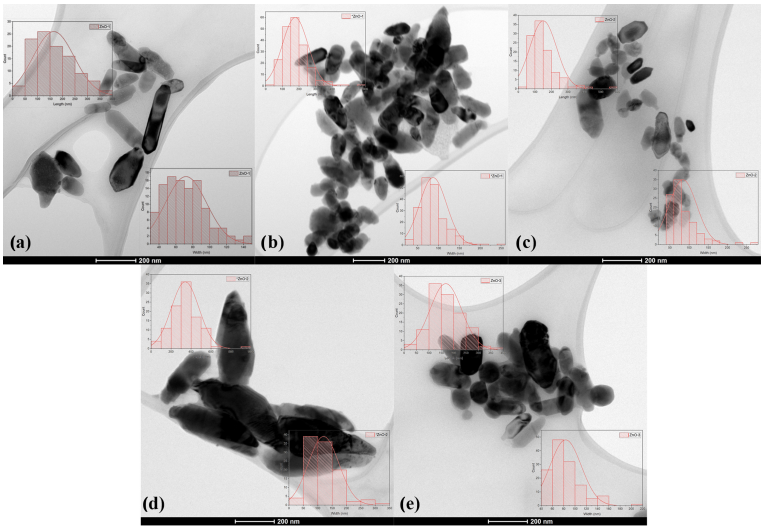


Figure 3. TEM images and histograms for each ZnO nanoparticle reaction of length and width: (**a**) ZnO-1, (**b**) *ZnO-1, (**c**) ZnO-2, (**d**) *ZnO-2, and (**e**) ZnO-3. For reactions with (*), the ammonium hydroxide was used.

Figure 3a depicts ZnO NPs of reaction ZnO-1, which have a well-defined column shape between length and width. From Figure 3b, we observe that the reaction *ZnO-1 generated ZnO NPs with high average size in both length and width and a slightly pointed shape. On the other hand, Figure 3c shows that reaction ZnO-2 produced ZnO NPs with a sharp morphology, and the difference between length and width is still well-defined. From Figure 3d, we report that reaction *ZnO-2 generated ZnO NPs with sharper morphology. Finally, Figure 3e illustrates that reaction ZnO-3 produced ZnO NPs with a well-defined morphology between length and width. The morphology indicates bigger growth on

reactions with ammonium hydroxide and a sharpy shape in the end of each nanoparticle, which may be due to hydroxyl ion enrichment. Thus, more faces are encouraged in their growth. On the other hand, reaction *ZnO-2 indicates that the longer the reaction time, a solution enriched in hydroxyl ions produces particles with a more dispersed size.

Table 3. Mean, standard deviation, and minimum and maximum size (nm) of the ZnO nanoparticles.

Reaction	Mean	Standard Deviation	Minimum	Maximum
		Length (nm)		
ZnO-1	164	82	40	389
*ZnO-1	177	77	44	572
ZnO-2	150	81	43	558
*ZnO-2	341	139	67	952
ZnO-3	168	64	49	363
		Width (nm)		
ZnO-1	72	24	33	145
*ZnO-1	87	32	31	256
ZnO-2	84	36	42	261
*ZnO-2	120	53	44	321
ZnO-3	83	28	43	209

Note: For reactions with (*), the ammonium hydroxide was used.

3.3. XRD

The X-ray diffractogram of ZnO NPs shows good quality in all reactions and does not present any impurity or precursor residue. Reflections match with the crystalline planes of the material structure and prove the formation of a hexagonal wurtzite phase (see Figure 4). Moreover, the peak broadening suggests the presence of small nanocrystals in samples. The mean crystallite size was calculated by the Scherrer equation, then the dislocation density was determined. Moreover, interplanar distance and wurtzite lattice constants were obtained and compared with the data registered JCPDS Card No. 36–1451 (See Tables S1 and S2). Therefore, the bond length from the tetrahedral of the wurtzite structure was calculated using the lattice constants, which proved the small or null presence of strain in the ZnO nanoparticles. Also, the band gap of the ZnO NPs was calculated using an effective mass model [31–34].

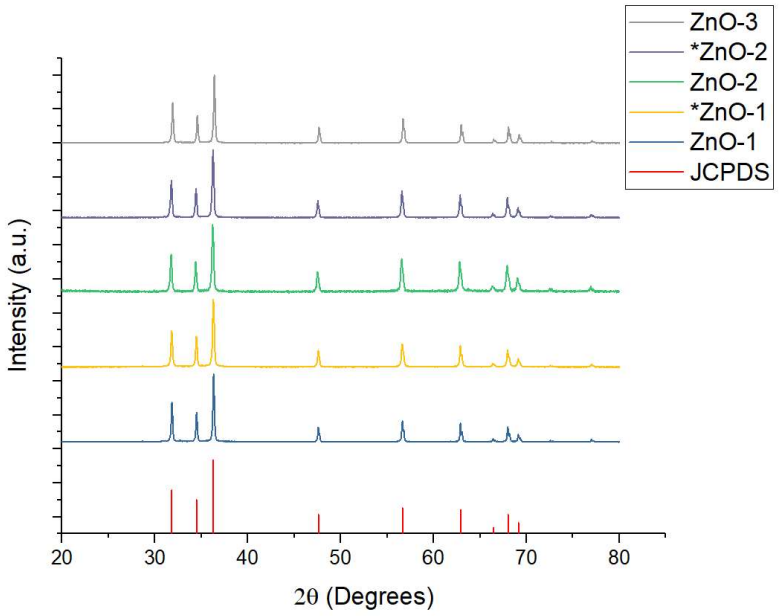


Figure 4. XRD patterns from each reaction.

3.3.1. Crystallite Size and Lattice Parameters

Crystallite is a domain in the material with the same crystallographic orientation. Its size has a significant influence on chemical, physical, and mechanical properties of metallic, ceramic, and polymeric nanomaterials [35]. Through the Scherrer equation, we determined an approximation of the average crystallite size of each reaction (See Table S3):

$$D = \frac{k\gamma}{\beta \cos\theta} \tag{1}$$

where D is the crystallites size, $k = 0.9$ is the Scherrer constant, $\gamma = 0.154183$ is the wavelength of the X-ray source in nanometers, β is the Full Width at Half Maximum (FWHM) in radians, and θ the peak position (in radians). All crystallite size were taken from each plane and an average size was obtained, D_m.

$$\delta = \frac{1}{D_m^2} \tag{2}$$

A dislocation defined as a line of structural discontinuities running throughout each crystal or grain [36] is defined per unit of volume as δ, and it was calculated with the average crystallite size for each reaction (Table 4). The presence of wide-reaching dislocations in the samples can produce significant peak broadening. Due to their implications, dislocation density and crystallite size are a main part of diffraction analysis [37].

Table 4. Crystallite size (nm) for each plane, mean size (nm), and dislocation density ∂ (nm^{-2}) for each ZnO NPs reaction.

Plane <h,k,l>	ZnO-1	*ZnO-1	ZnO-2	*ZnO-2	ZnO-3
D_m	30.82	32.03	29.5	30.99	34.69
$\delta\left(\times 10^{-4}\right)$	10.54	9.75	11.49	10.41	8.31

Note: For reactions with (*), the ammonium hydroxide was used.

The hexagonal closed packed arranged with zinc and the oxygen atoms coordinate with each other in an equivalent position. In addition, interplanar spaces from the wurtzite structure were calculated according to Bragg's law [38]. To obtain the lattice constants, we calculated the interplanar distance, which is a function of the unit cell parameters, and the Miller indices describe every set of crystallographic planes [39]. For a hexagonal crystal system, the inverse square of the interplanar distance has a relation with lattice constants a and c. Finally, a and c were calculated taking plane $(1\ 0\ 0)$ to obtain a, and $(0\ 0\ 2)$ to c.

Interplanar distances obtained from XRD match with the $(h\ k\ l)$ planes registered in the JCPDS card data. Moreover, Table 5 shows the lattice parameters calculated for every reaction, comparing them to the JCPDS card.

Table 5. Lattice parameters from XRD data and JCPDS data in Angstroms (Å).

Lattice Parameters	ZnO-1	*ZnO-1	ZnO-2	*ZnO-2	ZnO-3	JCPDS
a	3.26	3.25	3.26	3.25	3.24	3.25
c	5.22	5.21	5.22	5.21	5.19	5.21
c/a	1.6	1.6	1.6	1.62	1.6	1.60
V	47.9	47.6	47.9	47.78	47.17	47.62

Note: For reactions with (*), the ammonium hydroxide was used.

Lattice parameters ($a = b$), c, c/a, and volume V match with JCPDS card data. The c/a ratio has a correlation with the bond length L through the positional parameter in the wurtzite structure u, which is calculated in [38].

$$u = \frac{a^2}{3c^2} + 0.25 \tag{3}$$

Parameter u represents the relative shift of the anionic sublattice with respect to cationic sublattice in the c direction [40]. In the wurtzite structure of ZnO, zinc atoms occupy the special position 1/3, 2/3, 0, and oxygen occupies 1/3, 2/3, and u [40]. For and ideal wurtzite, the bond length for the c-axis and the parallel to a, b direction are equal (see Figure 5). To calculate the bond length into the c direction, L_c was used [40].

$$L_c = c \cdot u \tag{4}$$

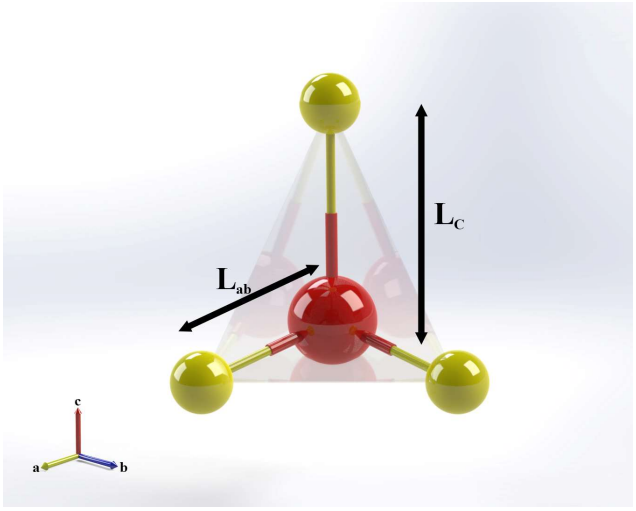


Figure 5. Bond length parallel to c, L_C—for ab, L_{ab}—in a tetrahedral Zn_4O structural unit. Red is oxygen and yellow is zinc.

To determine the other directions parallel to a and b, we used [41]

$$L_{ab} = \sqrt{\left(\frac{a^2}{3} + \left(\frac{1}{2} - u\right)^2 c^2\right)} \tag{5}$$

Table 6 summarizes the values obtained, comparing them with the reported Zn-O bond length in the unit cell.

Table 6. Values of u, L_C, and L_{ab} for each reaction. L_C and L_{ab} have units in Angstroms (Å).

Parameters	ZnO-1	*ZnO-1	ZnO-2	*ZnO-2	ZnO-3	References
u	0.3799	0.3799	0.3800	0.3799	0.3798	0.375 [42] **
L_c	1.9816	1.9773	1.9816	1.9800	1.9715	1.98 [41] **
L_{ab}	1.9816	1.9773	1.9816	1.9800	1.9715	1.9654 [38] 1.98 [41] ** 1.9767 [43]

Note: For reactions with (*), the ammonium hydroxide was used. ** For an ideal ZnO wurtzite.

3.3.2. Band Gap Estimation from Effective Mass Model Equation

The energy band gap can be determined by its relation to the crystallite size at quantum dot, E^n_{Gap}. This equation is due to the relation between electron and hole positions, induced by the Coulomb interaction [44]:

$$E^n_{Gap} = E^b_{Gap} + \frac{h^2}{8er^2}\left(\frac{1}{m_e} + \frac{1}{m_h}\right) - \frac{1.8e^2}{4\pi\varepsilon\varepsilon_o r} \quad (6)$$

where E^b_{Gap} is the energy gap on bulk ZnO (3.37 eV), r is the radius of the average crystallite size, m_e is the effective mass of the electron $(0.24\ m_o)$, m_h is the effective mass of hole $(0.45\ m_o)$, m_o is the rest mass of the electron $\left(9.11 \times 10^{-31} kg\right)$, ε is the relative permittivity (8.66), ε_o is the permittivity of free space $\left(8.854 \times 10^{-12} Fm^{-1}\right)$, h is the Planck's constant $\left(6.626 \times 10^{-34} Js\right)$, and e is the charge of the electron $\left(1.602 \times 10^{-19} C\right)$ [33]. Table 7 summarizes the values obtained by Equation (6).

Table 7. Band gap calculated by each reaction (eV).

Parameter	ZnO-1	*ZnO-1	ZnO-2	*ZnO-2	ZnO-3	Bulk
Band Gap	3.47	3.46	3.48	3.47	3.45	3.34

Note: For reactions with (*), the ammonium hydroxide was used.

The band gap analysis using the mass model equation shows dependence with the suggested synthesis. Due to the importance of the shape and size of the ZnO nanoparticles and their role in the band gap value, more characterizations must be implemented to obtain a relationship between proposed synthesis and band gap values.

3.4. Hysteresis Loop

Electrical characterizations were conducted in a powder sample that was compressed into a pill (see Figure 6). Then, silver paint was deposited on the top and the bottom of the ZnO powder pill to close the circuit. The material was polarized after interacting with an external electric field. The ZnO pill exhibited a 0.1 kV/cm coercive field, 3.47×10^{-4} μC/cm^2 remanent polarization, and 9.479×10^{-4} μC/cm^2 saturation polarization (see Figure 7). These results confirm the piezoelectric nature of the ZnO material.

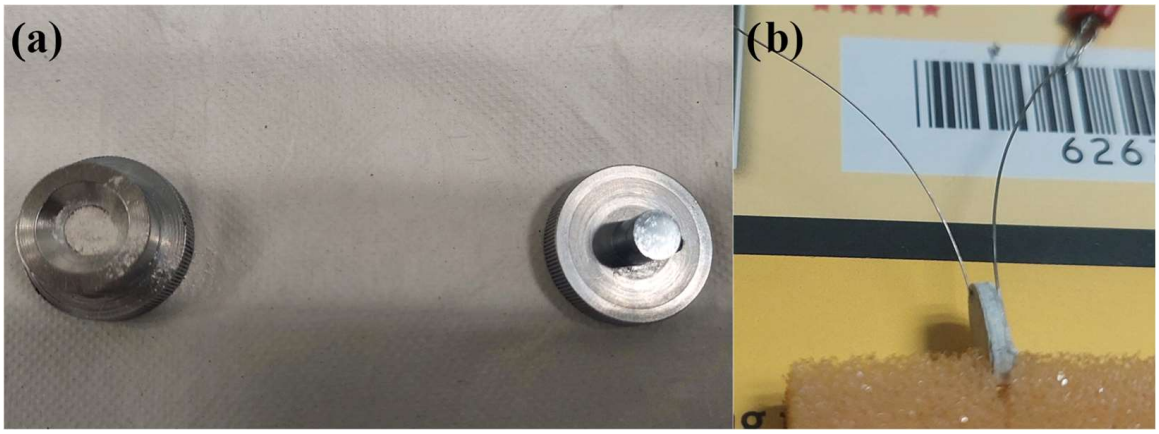


Figure 6. (**a**) ZnO powder before being compressed into a pill; (**b**) ZnO pill into a hysteresis characterization.

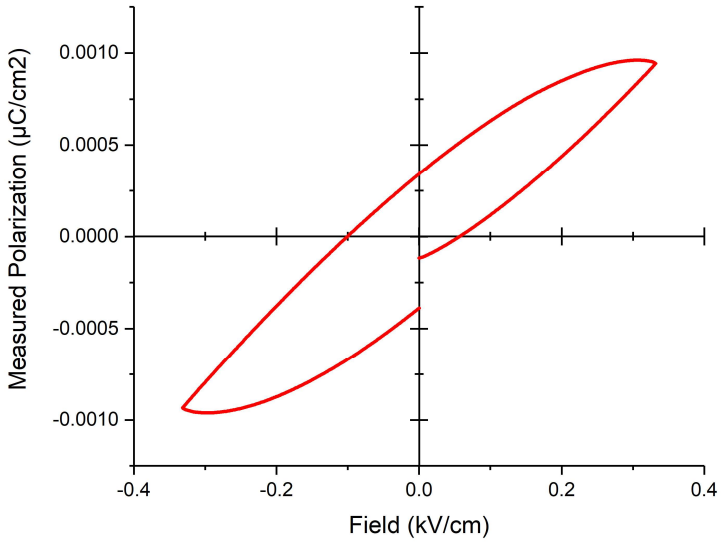


Figure 7. Measured polarization field hysteresis loops of ZnO powder pill.

3.5. Application

The MTI-2100 fotonic sensor is a fiber-optic measurement system (with a dual channel) that performs noncontact displacement and vibration measurements. By using fiber-optic technology, MTI-2100 does not apply load on the measurement target, and it is not affected by magnetic and electrical fields. We used this MTI-2100 fotonic sensor to measure the displacements of a beam that was fabricated using a steel substrate and a ZnO NP film synthetized with our method. This film was deposited on the outer surface of the steel substrate. A 20 MHz DDS function generator (BK PRECISION 4040B) and a digital oscilloscope (Agilent Technologies DSO3102A, Santa Clara, CA, USA) were used in the measurements of the displacements of the beam, which were generated by the supplied voltages. Square wave voltages from 1 to 10 V with a frequency of 1 Hz were supplied to the beam, which generated displacements of the beam (Figure 8a,b). The beam displacement was generated by the ZnO piezoelectric film. A second measurement of the beam was made with square wave voltages at 50 Hz and values from 1 to 10 V and 10 to 1 V (see Figure 9a,b). These measurements showed the piezoelectric effect of the ZnO NPs film that was deposited on the beam surface. When the supplied voltage is kept constant, the displacement of the beam is also kept constant. For voltages of 10 V at 1 and 50 Hz, the maximum displacement of the beam was close to 150 nm.

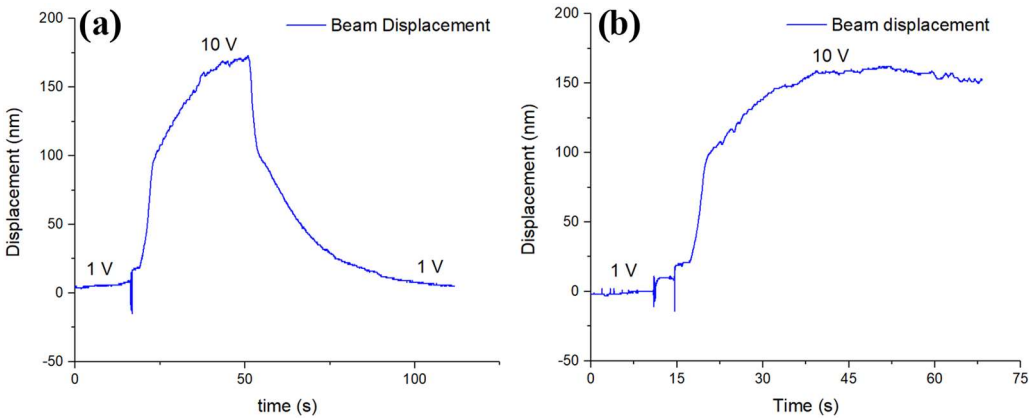


Figure 8. Displacement of a beam composed of a ZnO NPs film which was generated by square wave voltages at 1 Hz. Supplied voltages from (**a**) 1 to 10 and 1 V and (**b**) 1 to 10 V.

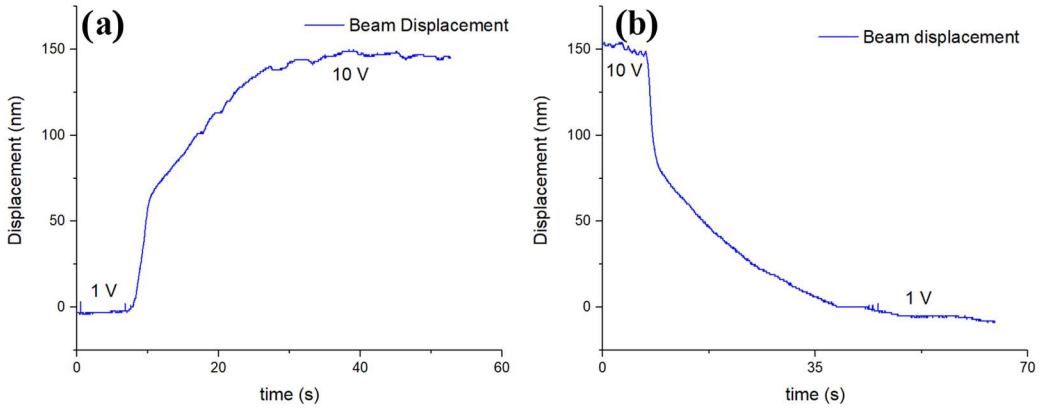


Figure 9. Displacement of a beam composed of a ZnO NPs film, which was generated by square wave voltages at 50 Hz. Supplied voltages from (**a**) 1 to 10 V and (**b**) 10 to 1 V.

Finally, the thickness of the ZnO NPs film was measured using KLA Tencor D-600. The thickness of the ZnO NPs film was around 7000 nm (see Figure 10).

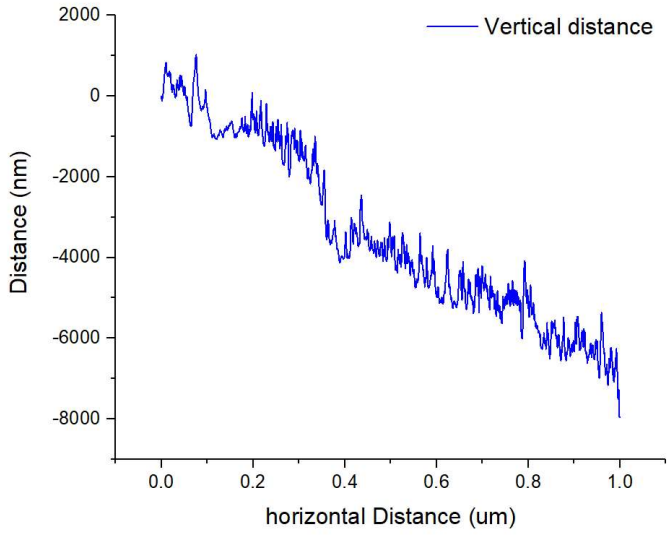


Figure 10. Measurements of the thickness of the ZnO NPs film.

4. Conclusions

We studied the impact of the reaction time and ammonium hydroxide addition on the morphology and properties of ZnO nanoparticles using a hydrothermal method. Consistent dimensions of the ZnO NPs were observed across different reactions, which demonstrated the repeatability of the proposed synthesis. The best morphological control of the ZnO NPs was achieved in reactions without ammonium hydroxide, probably due to enhanced growth along specific crystal faces. Furthermore, optical analysis reported a blue shift relative to bulk ZnO in most samples aside from reaction *ZnO-2, which showed a bathochromic shift that can be attributed to facile nucleation under modified conditions. XRD analysis confirmed high crystallinity and uniform crystallite sizes across reactions, regardless of hydroxide presence, while calculated band gaps aligned well with the literature values, reinforcing the reliability of the proposed synthesis. However, due to the influence of the shape and size of the ZnO nanoparticles in their electrical and mechanical properties, more characterizations must be developed to optimize the proposed synthesis.

Characterization of hysteresis loops of the ZnO NPs showed their piezoelectric properties in the reactions. Moreover, a ZnO NP film was deposited on the surface of a steel beam to measure its displacements due to piezoelectric effect under square wave voltages

of 1 and 10 V at 1 and 50 Hz. These ZnO NP films can be used to fabricate piezoelectric nanogenerators and self-powered sensors, as well as nanotransducers.

In future research work, we will investigate the thermal decomposition (TG-DSC) curves of the ZnO NPs films.

Supplementary Materials: The following supporting information can be downloaded at: https://www.mdpi.com/article/10.3390/technologies13010018/s1, Table S1: Peak points (degrees) for each reaction; Table S2: Interplanar distances from XRD data and JCPDS card in Angstroms (Å); Table S3: Crystallite size (nm) for each plane and for each reaction.

Author Contributions: Methodology and formal analysis, J.C.A.-Z.; investigation, A.S.L.-P.; conceptualization, C.G.-V.; formal analysis, J.R.-H.; investigation, C.N.A.-C.; visualization P.E.G.-C.; writing—original draft preparation, A.d.L.; writing—review and editing, A.L.H.-M. All authors have read and agreed to the published version of the manuscript.

Funding: Special thanks to the CONAHCYT for support through the CBF 2023–2024-4069 project.

Institutional Review Board Statement: Not applicable.

Informed Consent Statement: Not applicable.

Data Availability Statement: Data are contained within the article.

Acknowledgments: This research was developed at "Centro de Investigación en Química Aplicada" and "Universidad Veracruzana".

Conflicts of Interest: The authors declare no conflicts of interest.

References

1. Zhu, L.Y.; Ou, L.X.; Mao, L.W.; Wu, X.Y.; Liu, Y.P.; Lu, H.L. Advances in noble metal-decorated metal oxide nanomaterials for chemiresistive gas sensors: Overview. *Nano-Micro Lett.* **2023**, *15*, 89. [CrossRef]
2. Khan, M.M.; Matussin, S.N.; Rahman, A. Recent progress of phytogenic synthesis of ZnO, SnO_2, and CeO_2 nanomaterials. *Bioprocess Biosyst. Eng.* **2022**, *45*, 619–645. [CrossRef] [PubMed]
3. Le, A.T.; Ahmadipour, M.; Pung, S.Y. A review on ZnO-based piezoelectric nanogenerators: Synthesis, characterization techniques, performance enhancement and applications. *J. Alloys Compd.* **2020**, *844*, 156172. [CrossRef]
4. Podrezova, L.V.; Porro, S.; Cauda, V.; Fontana, M.; Cicero, G. Comparison between ZnO nanowires grown by chemical vapor deposition and hydrothermal synthesis. *Appl. Phys. A* **2013**, *113*, 623–632. [CrossRef]
5. Obreja, P.; Cristea, D.; Dinescu, A.; Romaniţan, C. Influence of surface substrates on the properties of ZnO nanowires synthesized by hydrothermal method. *Appl. Surf. Sci.* **2019**, *463*, 1117–1123. [CrossRef]
6. Rahman, W.; Garain, S.; Sultana, A.; Middya, T.R.; Mandal, D. Self-powered piezoelectric nanogenerator based on wurtzite ZnO nanoparticles for energy harvesting application. *Mater. Today Proc.* **2018**, *5*, 9826–9830. [CrossRef]
7. Mahanty, B.; Ghosh, S.K.; Jana, S.; Mallick, Z.; Sarkar, S.; Mandal, D. ZnO nanoparticle confined stress amplified all-fiber piezoelectric nanogenerator for self-powered healthcare monitoring. *Sustain. Energy Fuels* **2021**, *5*, 4389–4400. [CrossRef]
8. Kadam, V.; Jagtap, C.; Alshahrani, T.; Lokhande, P.; Al-Ahmed, A.; Patole, S.P.; Khan, F.; Pathan, H. Synthesis and characterization of ZnO nanoparticles and their application in dye-sensitized solar cells. *J. Mater. Sci. Mater. Electron.* **2023**, *34*, 1864. [CrossRef]
9. Salem, M.; Boussaid, A.; Hamida, M.B.B. Opto-electronic properties enhancement of silicon solar cells by iron doped ZnO nanoparticles. *Silicon* **2023**, *15*, 3543–3548. [CrossRef]
10. Hernández, M.R.; de León Santillán, A.; de Casas Ortiz, E.; Tavizón, S.F.; Moggio, I.; Arias, E.; Gallardo-Vega, C.A.; Silva, J.A.M.; Barriga-Castro, E.D. Hollow ZnO microspheres functionalized with electrochemical graphene oxide for the photodegradation of salicylic acid. *RSC Adv.* **2019**, *9*, 6965–6972. [CrossRef] [PubMed]
11. Canseco-Caballero, D.; Ledezma-Pérez, A.; Alvarado-Canché, C.; Castillo-Campohermoso, M.A.; Gallardo-Vega, C.; Barriga-Castro, E.D.; Herrera-May, A.L.; Saucedo-Salazar, E.; de León, A. ZnO nanorods functionalized with silver nanoparticles for electrochemiluminescence sensors in glyphosate detection. *Opt. Mater.* **2023**, *142*, 114101. [CrossRef]
12. Wang, L.; Choi, J. Improved recovery of NO_2 sensors using heterojunctions between transition metal dichalcogenides and ZnO nanoparticles. *Micro Nano Syst. Lett.* **2023**, *11*, 5. [CrossRef]
13. Benamara, M.; Rivero-Antúnez, P.; Dahman, H.; Essid, M.; Bouzidi, S.; Debliquy, M.; Lahem, D.; Morales-Flórez, V.; Esquivias, L.; Silva, J.P.B.; et al. Selective and rapid detection of acetone using aluminum-doped Zno-based sensors. *J. Sol-Gel Sci. Technol.* **2023**, *108*, 13–27. [CrossRef]

14. Wirunchit, S.; Koetniyom, W. ZnO nanoparticles synthesis and characterization by hydrothermal process for biological applications. *Physica Status Solidi (A)* **2023**, *220*, 2200364. [CrossRef]
15. Mohan, S.; Vellakkat, M.; Aravind, A.; Reka, U. Hydrothermal synthesis and characterization of Zinc Oxide nanoparticles of various shapes under different reaction conditions. *Nano Express* **2020**, *1*, 030028. [CrossRef]
16. Khudiar, S.S.; Nayef, U.M.; Mutlak, F.A.H. Preparation and characterization of ZnO nanoparticles via laser ablation for sensing NO_2 gas. *Optik* **2021**, *246*, 167762. [CrossRef]
17. Pimentel, A.; Ferreira, S.H.; Nunes, D.; Calmeiro, T.; Martins, R.; Fortunato, E. Microwave synthesized ZnO nanorod arrays for UV sensors: A seed layer annealing temperature study. *Materials* **2016**, *9*, 299. [CrossRef] [PubMed]
18. Tiwari, C.; Pandey, A.; Dixit, A. Precursor mediated and defect engineered ZnO nanostructures using thermal chemical vapor deposition for green light emission. *Thin Solid Film.* **2022**, *762*, 139539. [CrossRef]
19. Mocanu, A.; Rusen, E.; Diacon, A.; Damian, C.; Dinescu, A.; Suchea, M. Electrochemical Deposition of Zinc Oxide on the Surface of Composite Membrane Polysulfone-Graphene-Polystyrene in the Presence of Water Soluble Polymers. *J. Nanomater.* **2017**, *2017*, 1401503. [CrossRef]
20. Ben Amor, I.; Hemmami, H.; Laouini, S.E.; Mahboub, M.S.; Barhoum, A. Sol-gel synthesis of ZnO nanoparticles using different chitosan sources: Effects on antibacterial activity and photocatalytic degradation of AZO Dye. *Catalysts* **2022**, *12*, 1611. [CrossRef]
21. Aldeen, T.S.; Mohamed, H.E.A.; Maaza, M. ZnO nanoparticles prepared via a green synthesis approach: Physical properties, photocatalytic and antibacterial activity. *J. Phys. Chem. Solids* **2022**, *160*, 110313. [CrossRef]
22. Faisal, A.D.; Ismail, R.A.; Khalef, W.K.; Salim, E.T. Synthesis of ZnO nanorods on a silicon substrate via hydrothermal route for optoelectronic applications. *Opt. Quantum Electron.* **2020**, *52*, 212. [CrossRef]
23. Bouchoucha, I.; Salem, M.B.; Othmani, A.; Zouaoui, M. Effect on the structural, optical and electrical properties of Mn-doped ZnO nanobelts synthesized via the hydrothermal method. *Mod. Phys. Lett. B* **2020**, *34*, 2050177. [CrossRef]
24. Jevapatarakul, D.; Jiraroj, T.; Payungporn, S.; Chavalit, T.; Khamwut, A.; T-Thienprasert, N.P. Utilization of Cratoxylum formosum crude extract for synthesis of ZnO nanosheets: Characterization, biological activities and effects on gene expression of nonmelanoma skin cancer cell. *Biomed. Pharmacother.* **2020**, *130*, 110552. [CrossRef]
25. Al-Humaidi, J.Y.; Hagar, M.; Bakr, B.A.; Elwakil, B.H.; Moneer, E.A.; El-Khatib, M. Decorative multi-walled carbon nanotubes by ZnO: Synthesis, characterization, and potent anti-toxoplasmosis activity. *Metals* **2022**, *12*, 1246. [CrossRef]
26. Chu, H.O.; Wang, Q.; Shi, Y.-J.; Song, S.-G.; Liu, W.-G.; Zhou, S.; Gibson, D.; Alajlani, Y.; Li, C. Structural, optical properties and optical modelling of hydrothermal chemical growth derived ZnO nanowires. *Trans. Nonferrous Met. Soc. China* **2020**, *30*, 191–199. [CrossRef]
27. Elvira-Hernández, E.A.; Romero-García, J.; Ledezma-Pérez, A.; Herrera-May, A.L.; Hernández-Hernández, E.; Uscanga-González, L.A.; Jarvio-Cordova, V.A.; Hurtado, G.; Gallardo-Vega, C.; de León, A. Synthesis of ZnO Nanorod Film Deposited by Spraying with Application for Flexible Piezoelectric Energy Harvesting Microdevices. *Sensors* **2020**, *20*, 6759. [CrossRef]
28. Leprince-Wang, Y. *Piezoelectric ZnO Nanostructure for Energy Harvesting*; John Wiley & Sons: Hoboken, NJ, USA, 2015; Volume 1.
29. Baruah, S.; Dutta, J. Hydrothermal growth of ZnO nanostructures. *Sci. Technol. Adv. Mater.* **2009**, *10*, 013001. [CrossRef]
30. Talam, S.; Karumuri, S.R.; Gunnam, N. Synthesis, characterization, and spectroscopic properties of ZnO nanoparticles. *Int. Sch. Res. Not.* **2012**, *2012*, 372505. [CrossRef]
31. Misra, K.P.; Jain, S.; Agarwala, A.; Halder, N.; Chattopadhyay, S. Effective mass model supported band gap variation in cobalt-doped ZnO nanoparticles obtained by co-precipitation. *Semiconductors* **2020**, *54*, 311–316. [CrossRef]
32. Ghobadi, N. Band gap determination using absorption spectrum fitting procedure. *Int. Nano Lett.* **2013**, *3*, 2. [CrossRef]
33. Pushpanathan, K.; Sathya, S.; Chithra, M.J.; Gowthami, S.; Santhi, R. Influence of reaction temperature on crystal structure and band gap of ZnO nanoparticles. *Mater. Manuf. Process.* **2012**, *27*, 1334–1342. [CrossRef]
34. Lin, K.F.; Cheng, H.M.; Hsu, H.C.; Lin, L.J.; Hsieh, W.F. Band gap variation of size-controlled ZnO quantum dots synthesized by sol–gel method. *Chem. Phys. Lett.* **2005**, *409*, 208–211. [CrossRef]
35. Hassanzadeh-Tabrizi, S.A. Precise calculation of crystallite size of nanomaterials: A review. *J. Alloys Compd.* **2023**, *968*, 171914. [CrossRef]
36. Smallman, R.E.; Ngan, A.H.W. *Physical Metallurgy and Advanced Materials*; Elsevier: Amsterdam, The Netherlands, 2011.
37. Cullity, B.D.; Stock, S.R. *Pearson New International Edition: Elements of X-Ray Diffraction*; Prentice Hall: Saddle River, NJ, USA, 2014.
38. Bindu, P.; Thomas, S. Estimation of lattice strain in ZnO nanoparticles: X-ray peak profile analysis. *J. Theor. Appl. Phys.* **2014**, *8*, 123–134. [CrossRef]
39. Pecharsky, V.K.; Zavalij, P.Y. The powder diffraction pattern. In *Fundamentals of Powder Diffraction and Structural Characterization of Materials*; Springer: New York, NY, USA, 2009; pp. 151–202. [CrossRef]
40. Kumar, V.; Kumari, S.; Kumar, P.; Kar, M.; Kumar, L. Structural analysis by rietveld method and its correlation with optical propertis of nanocrystalline zinc oxide. *Adv. Mater. Lett.* **2015**, *6*, 139–147. [CrossRef]
41. Brehm, J.U.; Winterer, M.; Hahn, H. Synthesis and local structure of doped nanocrystalline zinc oxides. *J. Appl. Phys.* **2006**, *100*, 064311. [CrossRef]

42. Kriegner, D.; Assali, S.; Belabbes, A.; Etzelstorfer, T.; Holý, V.; Schülli, T.; Bechstedt, F.; Bakkers, E.P.A.M.; Bauer, G.; Stangl, J. Unit cell structure of the wurtzite phase of GaP nanowires: X-ray diffraction studies and density functional theory calculations. *Phys. Rev. B—Condens. Matter Mater. Phys.* **2013**, *88*, 115315. [CrossRef]
43. Seetawan, U.; Jugsujinda, S.; Seetawan, T.; Ratchasin, A.; Euvananont, C.; Junin, C.; Thanachayanont, C.; Chainaronk, P. Effect of calcinations temperature on crystallography and nanoparticles in ZnO disk. *Mater. Sci. Appl.* **2011**, *2*, 1302–1306. [CrossRef]
44. Brus, L. Electronic wave functions in semiconductor clusters: Experiment and theory. *J. Phys. Chem.* **1986**, *90*, 2555–2560. [CrossRef]

Disclaimer/Publisher's Note: The statements, opinions and data contained in all publications are solely those of the individual author(s) and contributor(s) and not of MDPI and/or the editor(s). MDPI and/or the editor(s) disclaim responsibility for any injury to people or property resulting from any ideas, methods, instructions or products referred to in the content.